Studies on interference effects of an odd CP state of the Higgs-boson with the Standard Model Z-boson

Frank Henry Nowak

Bachelorarbeit in Physik
angefertigt im Physikalischen Institut

vorgelegt der
Mathematisch-Naturwissenschaftlichen Fakultät
der
Rheinischen Friedrich-Wilhelms-Universität
Bonn

Februar 2025

Acknowledgements

I would like to thank Priv. Doz. Dr. Philip Bechtle and Prof. Klaus Desch for giving me the opportunity to write my bachelor's thesis in their group. Also, I would like to thank Luka Vomberg, Dr. Christian Grefe and Priv. Doz. Dr. Philip Bechtle for their help throughout the thesis. A special thank you to Florian Kirfel, Luka Vomberg, Murillo Vellasco for providing feedback to previous drafts and to all other members of the group for the nice working environment.
Thanks to my family for supporting me and thank you to my dog Kormi for providing comfort.

Contents

CHAPTER 1

Introduction

The Standard Model of particle physics (SM) is a well established theory in the research field of particle physics. It describes the interactions of fundamental matter and yields significant predictions which were confirmed in experiments, like the discovery of the Higgs-boson H [1, 2]. However, there are still some open questions to be answered that cannot be explained by the SM. For example, the measured baryon asymmetry or the presence of dark matter in the observable universe [3]. The attempt to accommodate these measurements into the SM led to the creation of new theories beyond the SM (BSM). Some of these BSM theories build upon the SM and extend it, often by the addition of new particles to the SM.

This thesis studies a BSM theory, that expands the Higgs sector of the SM minimally. This expansion is the odd CP state of the Higgs-boson and is called A [4]. Searches for A in the lower mass spectrum were done previously. However, interference between A and SM particles was not covered in the search [5]. A particle mass in this region is of particular interest, because of the measured excess at the CMS experiment in the cross section of $H \to \gamma\gamma$ at around 100 GeV [6, 7]. This thesis presents a qualitative study of possible interference effects of A with the Z-boson from the SM, as the result might help with the search for A by analyzing if interference effects must be accommodated for. If interference is present, corrections to the exclusions limits of the BSM theory must be made.

To investigate the interference, proton-proton collisions at a center-of-mass energy of 13.6 TeV are simulated. Events are analyzed, where both bosons, A and Z, are generated by vector boson fusion and decay to two tau leptons. All events are simulated via the Monte Carlo generator MadGraph5_aMC@NLO (MadGraph) for this process [8, 9], but these events are only evaluated on the truth level. Interactions of A are modelled via an effective theory, written with FeynRules [10, 11].

CHAPTER 2

Theory

In this chapter the SM and its limits are explained. Then BSM theories that incorporate A are elaborated and a short theoretical background on interference is given. Also different ways to produce Higgs-bosons at the LHC, which is explained in Chapter 3, are presented.

2.1 Standard Model

The Standard Model of particle physics is the best description of the interactions of fundamental particles thus far. It is build upon two particle types: Fermions and Bosons. Fermions are spin $1/2$ particles and they are separated into quarks and leptons. Quarks have color charge and fractional electric charge, while leptons carry an integer electric charge. Six quarks exist which are split into three generations of quark pairs, whereby masses increase along the generation. Similarly, leptons are split into three generations as well. They consist of the electron, the muon and the tau and each of them has a neutrino partner. The electron, muon and tau have an electric charge of $-e$ and they are sorted by their ascending mass value. The three neutrinos do not carry charge and are considered to be massless[1]. For each fermion an anti particle exists. These anti particles share the same mass but carry opposite charges.

Interactions between fermions are governed by the exchange of the second type of particles in the SM, the bosons. Unlike the fermions, bosons have an integer spin value. Specifically the photon, gluon, Z, and $W^{\pm}$ boson each have a spin value of 1. The gluon has a color charge and it is the exchange particle of the strong force. The theory which describes the color flow of the strong force is called Quantum Chromodynamics (QCD). Quarks are confined, due to the nature of the strong force, in bound states which are color neutral particles called hadrons.

The Z boson and the $W^{\pm}$ bosons are the carrier particles of the weak force. The Z is an electrically neutral particle, whereas the $W^{\pm}$ are electrically charged. Therefore the W bosons are responsible for the flow of electroweak currents. The W boson has a mass of (80.369 ± 0.013) GeV and the Z boson has a mass of (91.188 ± 0.002) GeV [13].

The photon is a neutral particle and it is the exchange particle of the electromagnetic force. The interactions of the photon and the gauge bosons Z, W are explained by the electroweak theory [3, 14]. All constituents of the SM along with their masses and electric charges are displayed in Fig. 2.1.

In the next paragraph the CP symmetry is elaborated shortly. A CP state can be assigned to a particle.

[1] This has been proven false in more recent discoveries like the neutrino-oscillations [12], but it does not matter for this work.

It refers to the behavior of a particles wave function under CP transformation. Here, the C denotes the charge conjugation, which transforms a particle into its antiparticle. The P denotes the parity transformation, which inverts the spatial components of the particles wavefunction. A CP even particle is invariant under CP transformations. Observations of the kaon decay show that the CP symmetry is violated [14, 15].

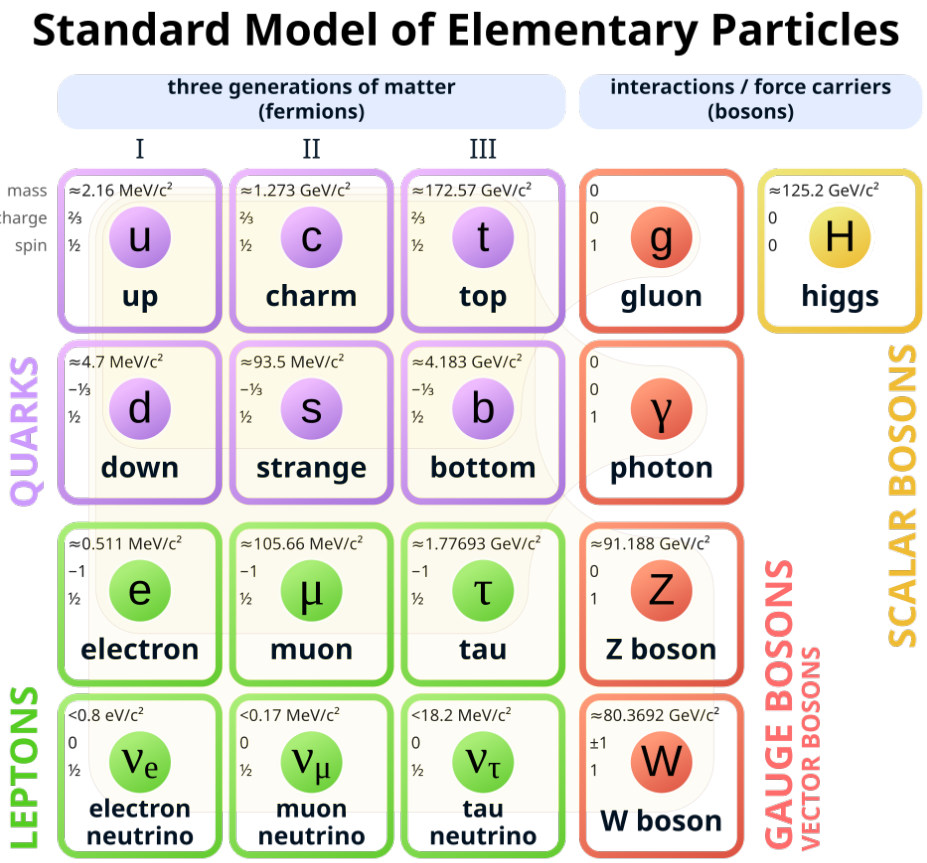

Figure 2.1: The Standard Model of particle physics is shown. It consists of 12 fermions and 5 bosons [16].

2.1.1 The Higgs particle

The SM, as discussed in Section 2.1 is not a complete theory, because the non zero mass of the gauge bosons causes the gauge symmetry to break. To solve this problem physicists Englert-Brout and Higgs theorized that another particle must exist and introduced the Higgs mechanism to the SM [17, 18]. Incorporating this mechanism, and the associated Higgs field into the SM gives an explanation that particles gain mass by coupling to the said field. Excitations of this field manifest an additional boson, the Higgs-boson. In 2012, the Higgs-boson was first measured at CERN [1, 2]. These measurements show that it is a scalar particle with a mass of 125 GeV and a width of 4 MeV [13]. All massive particles can couple to the Higgs-Boson with the coupling strength being directly proportional to their masses.

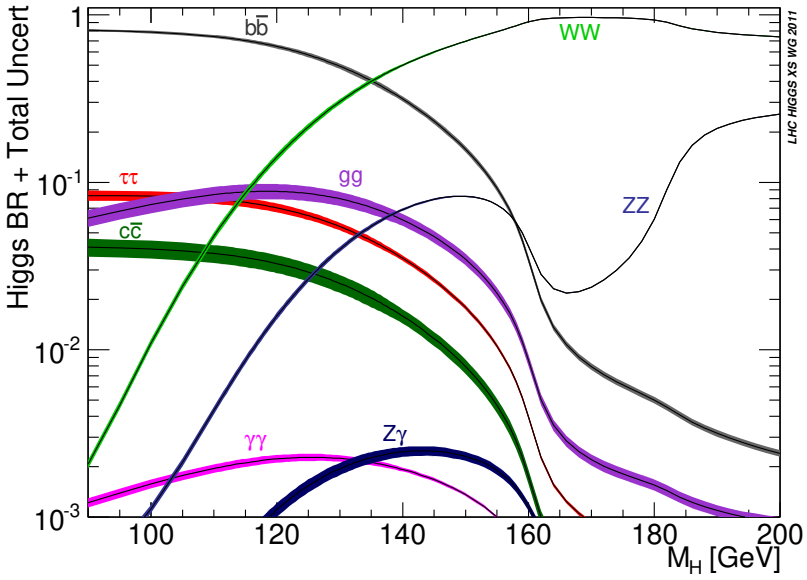

Figure 2.2: The branching ratios of the Higgs-boson, including their uncertainties can are displayed for a mass range of 90 to 200 GeV [19].

Therefore decays of the Higgs-boson to heavy particles are more favoured. Decay modes into massless particles are only possible through indirect decays, involving top quark or W/Z loops [3, 14].

The branching ratios of the Higgs-boson, predicted by the SM for different masses can be observed in Fig. 2.2. The favoured coupling of the Higgs-boson to larger masses can be seen. The decays into gauge bosons dominates in the higher mass range, starting at 160 GeV, which is twice the mass of the W-boson. In the lower mass range the decay to a pair of bottom quarks has the highest branching ratio. For this study the decay of the Higgs-boson to a pair of tau leptons is relevant. This decay is useful because the branching ratio stays constant below a mass of 120 GeV [19].

2.2 H production at the LHC

In this section the creation of the Higgs-boson at the LHC experiment is elaborated. That is why a brief summary about its production modes, in proton-proton collisions for a center-of-mass energy of 13.6 TeV, follows in this section. The LHC is explained in the Chapter 3.

The most dominant production modes are at the gluon-gluon fusion (ggF), the vector-boson fusion (VBF) and associated production with a vector-boson V or a pair of top quarks [20]. Feynman diagrams of these processes are displayed in Fig. 2.3. The ggF process has the highest cross section. It involves two initial gluons, which create a quark loop (usually a t) and finally a Higgs-boson. The second highest cross section belongs to the VBF mode where two initial quarks radiate a W-boson each that create a Higgs-boson. It is followed by the Higgs radiation process, where the Higgs is created as Bremsstrahlung from either a Z or W. Finally, the forth highest cross section is the one where the Higgs-boson is created with a pair of top quarks. In the experiment that study the Higgs-boson the required gluons or quarks stem from the proton-proton collisions [14, 21].

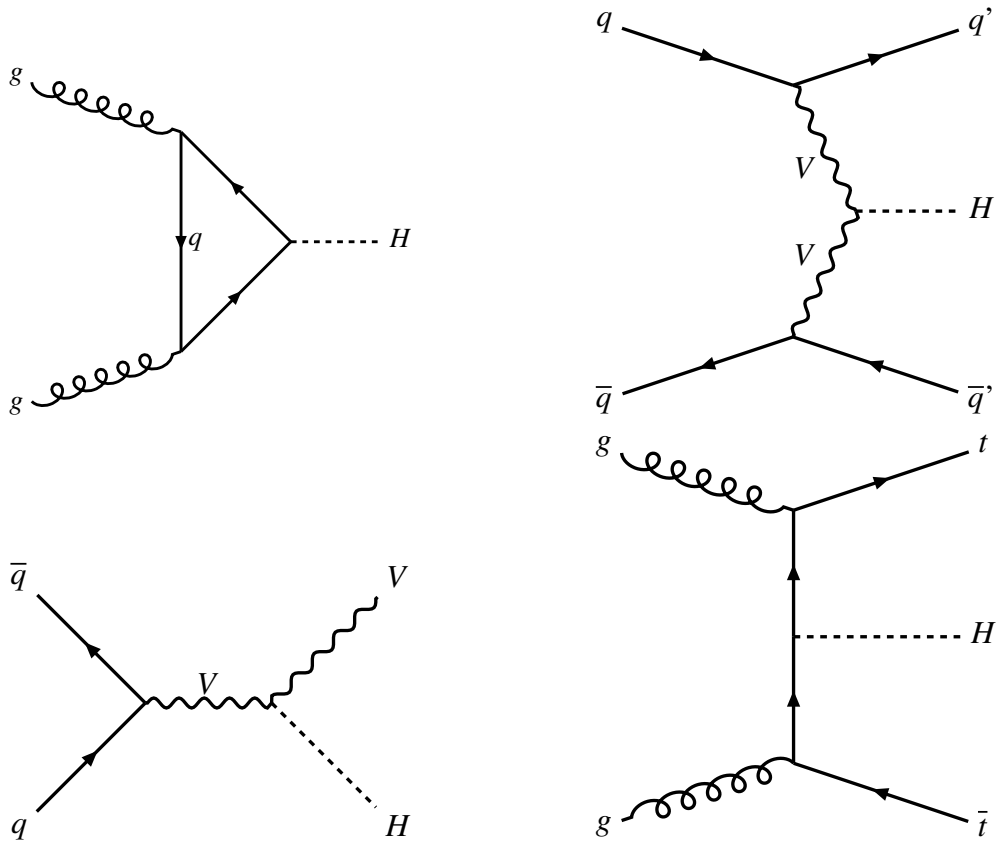

Figure 2.3: Feynman diagrams showing the production modes of the Higgs-boson. The V is either a Z or W [20].

2.3 Physics beyond the Standard Model

As mentioned before the SM does not answer all the questions within particle physics, for example it provides no answer to the baryon asymmetry in the observable universe. Additionally, the SM does not include the gravitational force and dark matter is not explained by the SM. Physical models that try to answer phenomena that are not explained by the SM are called Beyond Standard Model theories (BSM). Theories like the the Minimally Supersymmetric Standard Model (MSSM) could provide potential candidates for dark matter. It extends the Higgs sector by two Higgs-doublets [4]. However, it fails to provide an explanation for the measured excess at CMS. The Next-to-MSSM (NMSSM) includes another scalar to the MSSM and could explain the observed excess [22]. An addition to the theory is a particle A, which is a Higgs-boson with a CP odd state. It is contrasting the Higgs-boson from the SM that has an even CP state [4, 23].

2.4 Derivation of interference

The following section gives a short introduction on Quantum Field Theory (QFT), the framework behind the SM. Particular emphasis is placed on the definition of interference terms, relevant for this thesis.

Firstly, a Lagrangian is set up that encodes the possible couplings of particles. BSM theories include

more terms to the SM Lagrangian which enable new interactions between particles. Feynman diagrams, as referred to before, for example in Fig. 2.3, can be useful to illustrate the process and they consist of propagators, external legs and vertices. Propagators are internal lines that connect vertices to another. External legs connect to one vertex and belong to either incoming/initial states or outgoing particles/final states A vertex in QFT specifies the point in Feynman diagrams, where interacting particles couple to another [23].

A Feynman diagram describes the transition of an initial state ψ_i to a final state ψ_f. The matrix element $\mathcal{M}_{fi}$ (see Eq. (2.1)) is related to the transition probability of this process and features the physics of the theory or model, where $\mathcal{H}_{\text{int}}$ is the interaction Hamiltonian.

$$\mathcal{M}_{fi} = \langle \psi_f | \mathcal{H}_{\text{int}} | \psi_i \rangle \tag{2.1}$$

An essential observable of a process is the cross section σ which is the measurable probability distribution of the scattering process. It can be derived from Fermi's golden rule and it is calculated, apart from proportionality constants, by integrating the matrix element $|\mathcal{M}_{fi}|^2$ over the phase space Φ. The phase space Φ consists of the available final states ψ_f for each initial state ψ_i.

$$\sigma \propto \int \mathrm{d}\Phi \, |\mathcal{M}_{fi}|^2 \tag{2.2}$$

Only diagrams with the same initial and final states contribute to $\mathcal{M}_{fi}$. If multiple diagrams with corresponding matrix element $\mathcal{M}^k_{fi}$ contribute to a process, they must be added as $\mathcal{M}_{fi} = \sum_k \mathcal{M}^k_{fi}$. As $\mathcal{M}$ appears quadratically in Eq. (2.2), interference terms

$$\mathrm{Re}\left[\mathcal{M}^k_{fi}\left(\mathcal{M}^l_{fi}\right)^*\right] \text{ with } k \neq l$$

contribute to σ. Here, the $(z)^*$ denotes the complex conjugate of z and $\mathrm{Re}[z]$ the real part of z. The cross section σ yields terms like in Eq. (2.3).

$$\sigma \propto |\mathcal{M}_{fi}|^2 = \left|\sum_k \mathcal{M}^k_{fi}\right|^2 = \sum_k \left|\mathcal{M}^k_{fi}\right|^2 + 2 \times \sum_{k \neq l} \mathrm{Re}\left[\mathcal{M}^k_{fi}\left(\mathcal{M}^l_{fi}\right)^*\right], \tag{2.3}$$

where the second sum consists of the terms that contribute to the interference [3, 14, 24].

CHAPTER 3

Experiment

While this work contains no detector simulation, its results would be relevant for measurements done by the ATLAS detector or other high energy collider experiments. That is why a brief elaboration of the Large Hadron Collider (LHC) and the ATLAS experiment follows.

3.1 LHC

The LHC, located in Geneva, is a particle accelerator with the highest center-of-mass energy to date. Using a chain of pre-accelerators, it can accelerate two proton beams up to a beam energy of 6.8 TeV. These two beams are collided at four different points along the 27 km long circumference of the LHC, where four big experiments are located. These experiments are called ALICE (A Large Ion Collider Experiment), CMS (Compact Muon Solenoid), LHCb (Large Hadron Collider beauty) and ATLAS (A Toroidal LHC ApparatuS), which is of special interest for this thesis [25–27]. The ATLAS and CMS detector experimentally observed the Higgs boson in 2012 [1, 2].

3.2 ATLAS

The ATLAS detector consists of a multitude of detectors, that each specialize to measure certain particles. The inner detector consists of three components and it is encompassed by a magnetic field. The field is created by the solenoid, such that the field is aligned parallel to the beam axis [28].

First, the pixel detector is allocated closely to the beam axis and its measurements are used to predict the point, where the particle originates. The pixel detector is surrounded by the semiconductor tracker, which consists of four layers of silicon sensors. This allows high precision measurements of the particles trajectories. For charged particles, the trajectories are bend, because of the magnetic field. From these measurements, the momenta of these particles can be calculated by the detector. The last layer of the inner detector is the transition radiation tracker which consists of several layers of drift tubes. The transition radiation, which is different for lighter or heavier particles is used to determine the particle type [29].

The next component of the detector is a system of calorimeters that encapsulates the inner detector and the solenoid magnet. The calorimeters are used to measure the energy which is deposited by the particles. It is made up of a high density material which absorbs most particles energy except for neutrinos and

muons. The presence of neutrinos in processes is determined by evaluating the missing energy of particle events. The deposition of energy leads to a shower of new lower energetic particles. The first calorimeter is the Liquid Argon Calorimeter which is mainly used to measure the energy of photons and electrons. The Tile Hadronic Calorimeter is used to measure the energy of hadrons, which did not fully deposit their energy in the first calorimeter. It consists of steel tiles and plastic scintillators. Particles passing through these components use their energy in shower like processes [30].

The last part of the detector is a system, designated to measure muons. It is encompassed by the magnetic field that is created by the toroid [28]. They do not fully deposit their energy within the inner detector and calorimeter systems because of their mass which is 200 times higher than the electron mass. The muon spectrometer in the outer layer of the detector reconstructs the trajectories and momentum of muons [27, 31].

CHAPTER 4

Method

This chapter gives a small introduction to Monte-Carlo (MC) generators for particle collision simulations. The MC generator MadGraph is discussed along with the setup used for this study. These are not elaborated in detail, because that would be beyond the scope of this thesis (see citations for more information). This chapter focuses on the technical parts of the implementation instead.

4.1 Motivation for MC methods

This thesis analyzes simulated particle collisions, shortly termed MC events. Often the data obtained by experiments is limited. Therefore, MC simulation prove useful to either generate MC events to provide higher statistics or to generate MC events from theories, which can be tested with real data. These simulations consists of particle interactions which require the calculation of desired processes' cross sections (see Eq. (2.2)). It is a $3n-4$ dimensional integral, where n is the number of final state particles involved in the process. The calculation can become quite complex which requires non-analytical approaches. Therefore, numerical methods have been implemented in the form of MC techniques. To solve the integral, a large number N of small experiments are performed to approximate its result. Conducting an experiment means to sample four vectors randomly and uniformly out of the available set of final states Φ. The mean value of the matrix elements squared are then calculated for these random samples. This approximation is sufficient for some large number of experiments N. The error of this method scales like $N^{-1/2}$ [32, 33].

4.2 MC Generator

MC generators are staple software for analysis work at ATLAS. They manage the calculations required to simulate processes and generate MC events. One of them is MadGraph (MadGraph5_aMC@NLO), which is used for this thesis. MadGraph is a framework that utilizes features of different programs, but it does not generate the events on its own.

It is able to calculate the cross section of desired processes and the hard scattering particles or high-momentum partons [8, 9]. An UFO (Universal Feynman Output) model [34] that is written in the python programming language, describes the theory which is investigated. This file entails all the vertices and couplings of the theory. From the model, the Feynman rules for the calculation of the matrix

elements are derived with FeynRules [35]. The program Aloha [36] generates helicity wavefunctions which enables easier computation of the matrix elements. The calculated matrix elements are the input for the event generator.

The next step of the event generation is computed by the Pythia8 [37]. Pythia8 is used for the parton showers and hadronization of the decaying particles[1]. It includes the processes that take effect at lower energy scales. The output of this step is a list of stable particles that enter the detector. Here, stable particles are particles that exist long enough to enter the detector. Until this step, the simulation is based solely on theory predictions and incorporates no properties of the detector. The results of the simulation are called the truth MC events [39]. Still, the combination of MadGraph and Pythia8 is referred to as MadGraph throughout the thesis.

4.3 BSM model

The model that is used to simulate the MC events is the Higgs Characterisation model [10, 11, 40]. It encompasses all SM particles and couplings. In the model the Higgs-boson has a variable CP state depending on the parameter α. Here, α is the mixing angle between the odd CP state ($s_\alpha = \sin(\alpha) = 1$) and even CP state ($c_\alpha = \cos(\alpha) = 1$). For $c_\alpha = 1$ the Higgs-boson features the properties of the SM. The relation $\sin^2(\alpha) + \cos^2(\alpha) = 1$ is automatically enforced by the model. An effective Lagrangian entails the couplings of the Higgs-boson, which define its CP state. Therefore, the Lagrangian can be expressed as

$$\mathcal{L} = \mathcal{L}_{\text{SM}} + \mathcal{L}_{\text{effective}}. \tag{4.1}$$

The parameters of Higgs-boson are set to $c_\alpha = 0$ and $s_\alpha = 1$ to model a CP odd Higgs-boson, referred to as A. The mass of A can be varied in the model and it is set onto the Z peak to 92 GeV to allow interference between the Z and A. The coupling of A to a pair of W-bosons can be included by setting the parameter κ_{AWW} to 1. To enhance the signal this parameter is set to $\kappa_{AWW} = 5$.

4.3.1 MadGraph simulations

This section focuses on the simulated interfering diagrams that are analyzed. MadGraph generates Feynman diagrams from a syntax that is written in the Python programming language. They restrict the hard scattering processes that are investigated. In the appendix Chapter A the technicalities of MadGraph are elaborated to achieve the desired diagrams.

The diagrams that are investigated can be seen in Fig. 4.1. They display the creation of A or Z using the VBF mode and their decay to a pair of tau leptons. Here, it is important to mention that it is CP violating to have a coupling of an CP odd particle to two CP even particles on the tree level. However, it is possible for A to couple to WW through indirect fermion loops [4].

The initial particles are set to be $u\bar{u}$ that are converted to a $d\bar{d}$ pair by radiating two W bosons. In the ATLAS experiment the process $pp \to \tau^+\tau^-$ is observed. However, to maximize the signal generated by one particular matrix element the initial and final states are fixed. $u\bar{u} \to \tau^+\tau^-$ is a sub process of $pp \to \tau^+\tau^-$.

A motivation why the VBF mode is used to generate A follows in this paragraph. These measurements stem from the SM Higgs-boson, but it still affects A because A inherits the SM couplings of the

[1] The parton density functions were handled by `LHAPDF6` [38].

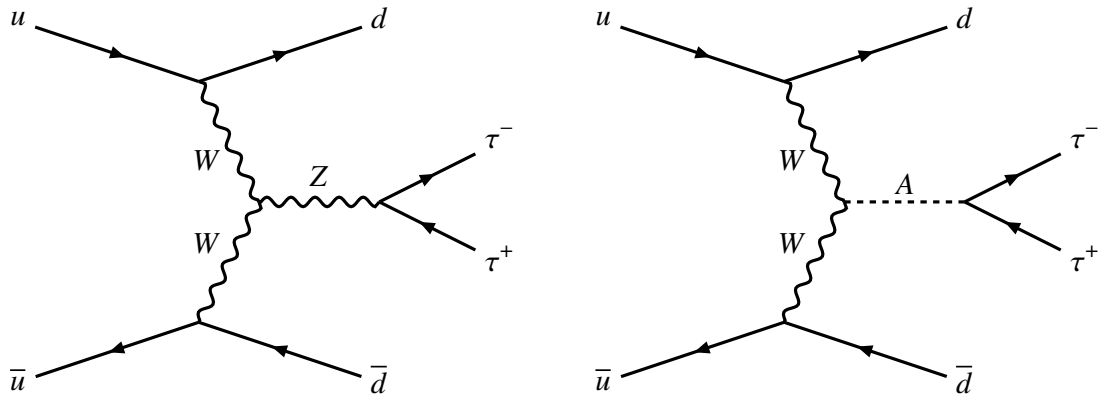

(a) Z created from VBF process

(b) A created from VBF process.

Figure 4.1: Feynman diagrams showing the interfering processes. In Fig. 4.1(a) a Z-boson is shown that is created by VBF and it decays to a τ pair. In Fig. 4.1(b) A is shown that is created by VBF and it decays to a pair of tau leptons.

Higgs-boson in this simulation. The total uncertainties of the cross section for the different production processes of the Higgs-boson in the SM can be read in Table 4.1 [20]. The VBF generating mode yields the most precise cross section.

Table 4.1: Best-fit value and total uncertainty for the cross section for different production modes of the Higgs-boson [20].

Production mode	ggF	ttH	VBF	VH
Best-fit value	0.92	0.77	1.04	0.98
Total uncertainty	± 0.30	± 0.97	± 0.18	± 0.66

In the following, the simulation which features the interference of the diagrams in Fig. 4.1 is referred to as coherent signal or coherent simulation. The simulation, where the MC events are generated in a way as if the diagrams do not belong to one process, is called incoherent signal or incoherent simulation. The difference is elaborated using the cross section from Eq. (2.3).

The resulting cross section for the coherent signal takes the form in equation Eq. (4.2).

$$\sigma \propto |\mathcal{M}_{fi}|^2 = |\mathcal{M}_A|^2 + |\mathcal{M}_Z|^2 + 2 \times \mathrm{Re}\left[\mathcal{M}_A \left(\mathcal{M}_Z\right)^*\right] \tag{4.2}$$

$\mathcal{M}_A$ denotes the matrix element of the diagram where A is in the s-channel and $\mathcal{M}_Z$ denotes the matrix element of the diagram where the Z is in the s-channel.

For the incoherent signal the diagrams are created separately. Generating them in one simulation keeps the relative abundances of Z and A. Therefore, no normalization using branching ratios and cross sections of the processes $pp \to A$ or $pp \to Z$ is required. The cross section can be written as in Eq. (4.3).

$$\sigma = \sigma_A + \sigma_Z \propto |\mathcal{M}_A|^2 + |\mathcal{M}_Z|^2 \tag{4.3}$$

The difference between Eq. (4.3) and Eq. (4.2) is only the interference contribution. To reconstruct the

mass of the particle in the s-channel, the total truth 4-momenta of the two τ leptons are quadratically summed up.

CHAPTER 5

Results

The outputs of the simulations are discussed in this chapter, firstly for a particle width of $\Gamma_A = 4\,\text{MeV}$ and then for $\Gamma_A = 40\,\text{MeV}$. For each set of parameters the coherent simulation is compared with the incoherent simulation. To explore the interference the cross section is evaluated differentially in $m_{\tau\tau}$ for each simulation. As the incoherent and coherent simulation are the same except for the interference contributions, it is sufficient to analyze the differential cross section. In order to compare the shapes of the incoherent and coherent simulation, the ratio of their differential cross section is calculated. To analyze the ratio, a constant function is fitted to the ratio within a narrow mass range around the A peak, using an ordinary least squares fit. A χ^2-test is performed on a narrow mass range around the A peak. This way, the null-hypothesis is tested that the ratio yields perfect unity, i.e. the signals are identical and there is no significant interference.

5.1 Analysis of interference effects between A and Z

In these simulations the width of A is equal to the width of the SM Higgs-boson. The differential cross section is shown in Fig. 5.1(a). A narrow peak can be observed on top of a broader peak for the coherent and incoherent signals. The broader peak is the Z peak at 91 GeV and the narrow peak is the peak of the A at 92 GeV. The shapes of the MC events for both signals look similar.

Since the A has a width of $\Gamma_A = 4\,\text{MeV}$, the observed energy interval is set to a narrower window. The histogram in Fig. 5.1(b) shows a narrow window around the mass of the A, where the mass values are in the range of $M_A \pm 5\,\Gamma_A$. Again, the shapes of the coherent and incoherent simulation agree with each other.

The difference between the coherent and incoherent signal is to be evaluated. In order to do that, the two signals are divided by each other as shown in Eq. (5.1). The ratio $\mathcal{R}$ is close to unity in the case that the signals are identical, implying that interference effects are small. If $\mathcal{R} > 1$ for a range of mass values, it indicates destructive interference and if $\mathcal{R} < 1$, the signals interfere constructively. The error is shown in Eq. (5.2).

$$\mathcal{R} = \frac{\sigma_{\text{incoherent}}}{\sigma_{\text{coherent}}} \tag{5.1}$$

$\sigma_{\text{incoherent}}$ denotes the differential cross section of the incoherent simulation and σ_{coherent} denotes the

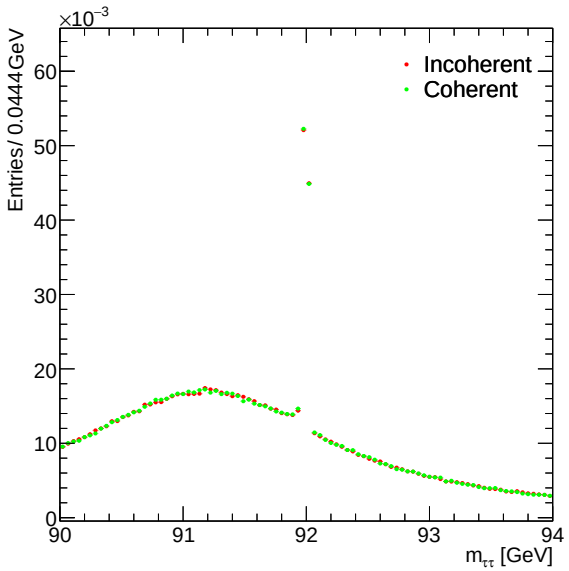

(a)

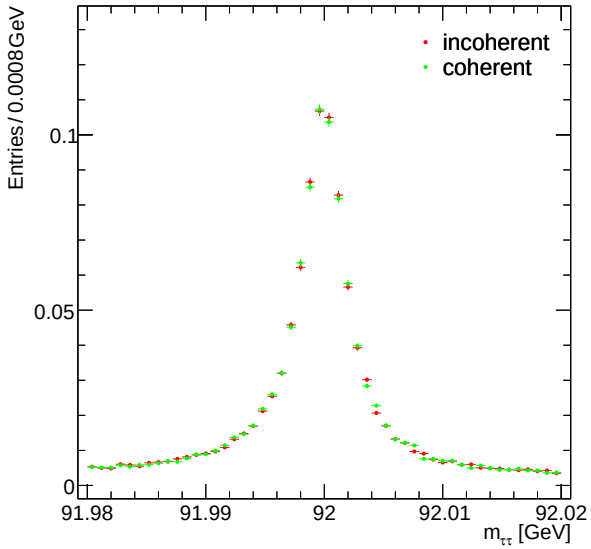

(b)

Figure 5.1: Two histograms showing the differential cross section of the coherent and incoherent simulation. In (a) the mass range is set from 90 to 94 GeV. The figure in (b) is a zoomed-in histogram of (a). Here, a narrow mass scale around the A peak can be observed. On the x axis the invariant mass of the two τ system is displayed. Whereas on the y axis the differential cross section in arbitrary units per energy interval is shown. The errors are of purely statistical origin and both histograms are normalized.

differential cross section of the coherent simulation.

$$\Delta\mathcal{R} = \sqrt{\left(\frac{\Delta\sigma_{\text{incoherent}}}{\sigma_{\text{coherent}}}\right)^2 + \left(\frac{\sigma_{\text{incoherent}} \cdot \Delta\sigma_{\text{coherent}}}{(\sigma_{\text{coherent}})^2}\right)^2} \tag{5.2}$$

The ratio $\mathcal{R}$ can be seen in Fig. 5.2. The values within one width of A around the central value of

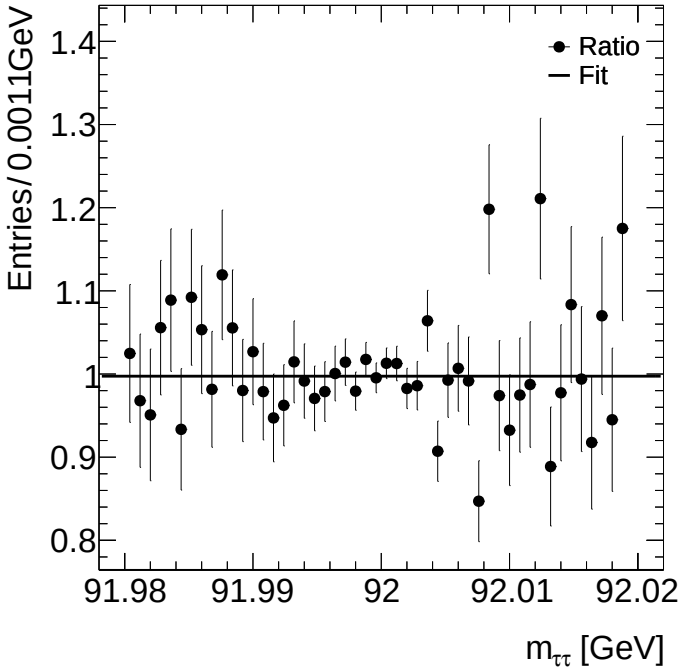

Figure 5.2: A histogram showing the ratio of the coherent and incoherent simulation, according to Eq. (5.1), from Fig. 5.1(b). On the x axis the invariant mass of the two τ system is displayed. Whereas on the y axis the ratio in arbitrary units per energy interval is shown. The errors are statistical errors.

92 GeV show substantially smaller statistical errors, due to the larger statistics in the bins at and around the A-peak compared to the tails. The values outside of that mass range show larger fluctuations and have larger errors. The reason for that is the smaller statistics for these bins. This can be observed in Fig. 5.1(b). To decrease this error, more events could be generated, however, the storage size of the generated samples quickly becomes an issue. A more efficient way to generate and pre-select the events, for example via a mass cut around the A-mass would need to be implemented to yield further decreases in the statistical error.

To quantify the shape of the ratio, a fit is performed to the MC events with the null-hypothesis that the ratio is equal to a constant value.

$$f(\mathcal{R}) = a \tag{5.3}$$

A least squares fit for the values in the range $M - 5\,\Gamma_A$ and $M + 5\,\Gamma_A$ is performed. The fit yields $\chi^2 = 54$ with a number of degrees of freedom (ndf) of 48. The fit function is shown in Eq. (5.3) and the values of the ratio are distributed around a constant $a = 0.997 \pm 0.006$. The χ^2-test gives a p-value of 25 %.

Since the choice of fit-range is arbitrary, the test was repeated multiple times in different ranges. These additional tests yield similar results, confirming the stability of the method against the fit-range.

5.2 Analysis of interference effects between A and Z for a larger width

In this simulation the width of A is scaled up by a factor of 10, to study if the width has an effect on possible interference. The differential cross section of the coherent and incoherent simulation can be observed in Fig. 5.3. Here, the A peak is not as defined as in Fig. 5.1(b). Also, a higher count of Z events can be observed. The shapes of the incoherent and coherent signal agree with each other. The overall height of the A peak in relation to Z is smaller than before due to the larger width of A. To have a larger contrast of the A peak, the coupling of A to WW,i.e. κ_{AWW} could have been increased as well.

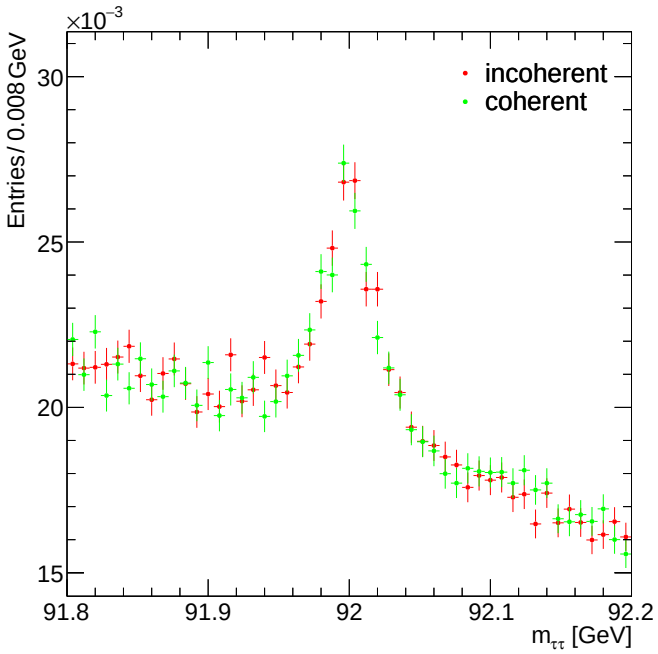

Figure 5.3: A histogram showing the differential cross section of the coherent and incoherent simulation for a width of A of $\Gamma_A = 40$ MeV. On the x axis the invariant mass of the two τ system is displayed. Whereas on the y axis the differential cross section in arbitrary units per energy interval is shown. The errors are statistical errors and the histograms are normalized. A simulation of 1.2 million MC events was performed for the coherent and incoherent signal.

Again to measure the difference between the shapes of the incoherent and coherent simulation, the ratio of them is computed for values in between $M_A - 5\,\Gamma_A$ and $M_A + 5\,\Gamma_A$. This range is chosen to stay consistent with the ratio graph from the smaller width scenario. It is displayed in Fig. 5.4 and a constant function is fitted to the ratio. The ratio is distributed around $a = 0.998 \pm 0.005$ and the fit yields $\chi^2 = 44$ with ndf of 48. The resulting p-value is at 64 %.

Since the choice of the fitted mass range is arbitrary, another χ^2-test is performed on a mass range of $M_A - 2\,\Gamma_A$ and $M_A + 2\,\Gamma_A$. The result is a value of $\chi^2 = 18.5$ with a ndf of 19. This way a p-value of

49 % is achieved. In Fig. B.1 in the appendix the values of the ratio can be observed.

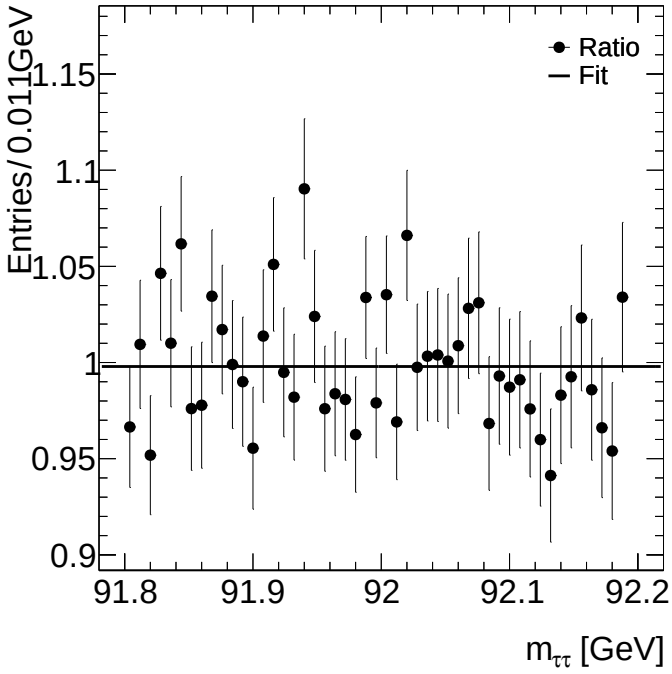

Figure 5.4: A histogram showing the ratio of the coherent and incoherent simulation, according to Eq. (5.1), with values from Fig. 5.3 for a width of $\Gamma_A = 40\,\text{GeV}$. On the x axis the invariant mass of the two τ system is displayed. Whereas on the y axis the ratio in arbitrary units per energy interval is shown. The errors are statistical errors and a fit with a constant value can be observed.

5.3 Discussion and outlook

The p-values for both width scenarios imply no significant deviation of the incoherent signal from the coherent signal. The p-value was smaller for a width of $\Gamma_A = 4\,\text{MeV}$ than for $\Gamma_A = 40\,\text{MeV}$. In the simulation where $\Gamma_A = 40\,\text{MeV}$, the A peak was less defined than in the simulation where $\Gamma_A = 4\,\text{MeV}$. To compensate this, a larger coupling κ_{AWW} could be chosen for future testing. The hypothesis that the incoherent and coherent signal are identical cannot be discarded. Therefore, no interference can be measured for this particular setup.

To measure the interference more precisely, a larger amount of MC events could be simulated to reduce the statistical error of the ratio $\mathcal{R}$. The interference effects on smaller mass scales could also be investigated. To search in smaller scales, more fine-grained binning could be set up. However, even more MC events must be generated to have a good resolution of these scales. Mass cuts to the combined mass of the tau leptons could be applied in the simulation to enforce MadGraph to compute MC events within range of the A peak and increase computational efficiency. However, the experimental resolution of the ATLAS detector is already higher than the width of the Higgs-boson, which begs the question, whether interference effects on such small scales can even be measured.

Another reason for these findings could be the VBF channel for A and Z. These diagrams could yield vanishing or only small interference contributions. To explore the interference further, one could set up a simulation where the A is created via the ggF process or other generating modes of the Higgs-boson. Also, it would be interesting to try simulating the process in another MC generator to test for interference.

CHAPTER 6

Conclusion

Interference effects between BSM and SM particles can provide useful information for the search of new physics. These effects could alter the measured observables and give corrections to the exclusion limits of BSM theories. This work provides a first look into the exploration of interference effects between the CP odd H-boson and the Z-boson. This odd CP state of the Higgs-boson is referred to as A.

The main part of this work targeted the correct implementation and comprehension of the MC generator MadGraph [8, 9]. A deeper understanding of MadGraph was achieved and a simulation with interfering diagrams was set up. The Higgs-boson A was simulated with the Higgs characterisation model [10, 11]. MC simulations to test for interference between A and Z were carried out for a mass $M_A = 92\,\text{GeV}$ and two width scenarios $\Gamma_A = 4\,\text{MeV}$ and $\Gamma_A = 40\,\text{MeV}$.

A and Z were generated in the VBF mode and decayed to two tau leptons. The initial and final states were fixed to enhance the signal and to exclude all the different combinations of quarks. MadGraph was set up to produce an coherent and incoherent simulation of the specific diagrams Fig. 4.1 for each set of parameters. In the coherent simulation interference between these diagrams was possible and in the incoherent simulations interference was excluded. To investigate the difference of these signals, the ratio of the differential cross sections of the incoherent and coherent simulation was evaluated, shown in Eq. (5.1).

A least squares fit was performed on a narrow mass range ($M - 5\,\Gamma_A$ to $M + 5\,\Gamma_A$) around the A peak with a constant function to observe the deviation of the incoherent from the coherent signal. A χ^2-test was performed to measure the likelihood that interference is present. However, the processes did not show any interference. The p-value for the width of $\Gamma_A = 4\,\text{MeV}$ is at 25 %. For the larger width of $\Gamma_A = 40\,\text{MeV}$, the p-value is at 49 % for a mass range of $M - 2\,\Gamma_A$ to $M + 2\,\Gamma_A$ and the p-value is at 64 % for a mass range of $M - 5\,\Gamma_A$ to $M + 5\,\Gamma_A$.

Therefore, ratio is close to unity for the considered mass scale and does not show any underlying shape. In the second width scenario, the A peak is not as defined as in the first case, which can explain the higher p-value. To enhance the A peak, a larger coupling of κ_{AWW} can be chosen. Also, to reduce the statistical error of the ratios, a larger number of MC events could be generated. To increase computational efficiency, mass cuts could be applied to the tau leptons, because only a fraction of MC events are analyzed. To build upon the thesis, one could consider another generating mode of A, for example the ggF process.

APPENDIX A

Method

A.1 MadGraph input

In the following the technical aspects of MadGraph and its syntax are elaborated to generate the requested Feynman diagrams. In MadGraph each vertex has coupling orders, depending on what kind of underlying theory the coupling belongs to. The contributions of $\mathcal{L}_{\text{SM}}$ in $\mathcal{L}$ (see Eq. (4.1)) have the QCD or QED coupling orders. These denote either couplings of the SM that belong to the theory of Quantum Chromodynamics (QCD) or Quantum Electrodynamics (QED) [23]. The contributions of $\mathcal{L}_{\text{effective}}$ in $\mathcal{L}$ have the QNP (NP for new physics) coupling order. The order of the CP odd coupling of A with two W bosons from $\mathcal{L}_{\text{effective}}$ is defined as QWA. The vertex of two W and one Z only has one coupling and its order is defined as QWZ. One coupling order is defined as QSM that belongs to Higgs radiation Feynman diagrams, which is not required. This way one can setup up MadGraph to only allow desirable diagrams, as shown in Fig. 4.1.

The input of MadGraph is shown below, where the simulation which features the interference of the diagrams is referred to as coherent signal or coherent simulation. The simulation, where the MC events are generated in a way as if the diagrams do not belong to one process, is called incoherent signal or incoherent simulation.

- For the coherent signal the input is:

  `"generate u u~ > d d~ ta+ ta- QCD=0 QED=3 QSM=0"`

- For the incoherent signal the input is:

  ”`generate u u~ > d d~ ta+ ta- QCD=0 QED=3 QSM=0 QWZ=0`

  `add process u u~ > d d~ ta+ ta- QCD=0 QED=3 QSM=0 QWA=0`”

APPENDIX B

Results

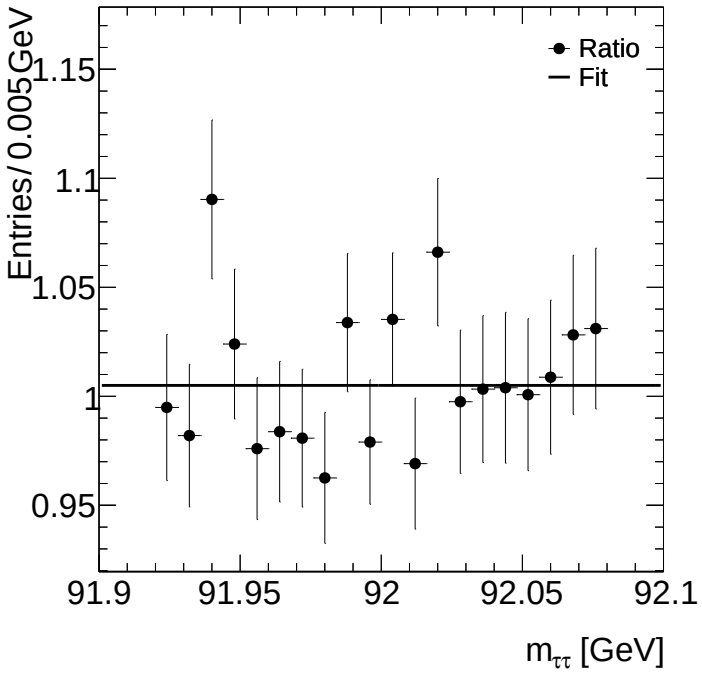

Figure B.1: A histogram showing the ratio of the coherent and incoherent simulation, according to Eq. (5.1), with values from Fig. 5.3 for a width of $\Gamma_A = 40\,\text{GeV}$. Only values within a mass of $M_A - 2\,\Gamma_A$ and $M_A + 2\,\Gamma_A$ are considered. On the x axis the invariant mass of the two τ system is displayed. Whereas on the y axis the ratio in arbitrary units per energy interval is shown. The errors are statistical errors and a fit with a constant value can be observed.

Bibliography

[1] The ATLAS Collaboration, *Observation of a new particle in the search for the Standard Model Higgs boson with the ATLAS detector at the LHC*, Physics Letters B **716** (2012) 1, ISSN: 0370-2693, URL: https://www.sciencedirect.com/science/article/pii/S037026931200857X (cit. on pp. 1, 3, 7).

[2] The CMS Collaboration, *Observation of a new boson at a mass of 125 GeV with the CMS experiment at the LHC*, Physics Letters B **716** (2012) 30, ISSN: 0370-2693, URL: https://www.sciencedirect.com/science/article/pii/S0370269312008581 (cit. on pp. 1, 3, 7).

[3] M. Thomson, *Modern Particle Physics*, Cambridge University Press, 2013, ISBN: 9781107034266 (cit. on pp. 1, 2, 4, 6).

[4] J. F. Gunion, H. E. Haber, G. Kane and S. Dawson, *Frontiers in Physics: The Higgs Hunter's Guide*, Addison-Wesley Publishing Company, 1990, ISBN: 0-201-50935-0 (cit. on pp. 1, 5, 10).

[5] The ATLAS Collaboration, *Search for a light CP-odd Higgs boson decaying into a pair of τ-leptons in proton-proton collisions at $\sqrt{s}$= 13 TeV with the ATLAS detector*, Journal of High Energy Physics **81** (2024), ISSN: 1029-8479, URL: https://doi.org/10.1007/JHEP12(2024)126 (cit. on p. 1).

[6] The CMS Collaboration, *Search for a standard model-like Higgs boson in the mass range between 70 and 110 GeV in the diphoton final state in proton-proton collisions at $\sqrt{s}$=8 and 13 TeV*, Physics Letters B **793** (2019) 320, ISSN: 0370-2693, URL: https://www.sciencedirect.com/science/article/pii/S0370269319302904 (cit. on p. 1).

[7] The CMS Collaboration, *Searches for additional Higgs bosons and for vector leptoquarks in $\tau\tau$ final states in proton-proton collisions at $\sqrt{s}$ = 13 TeV*, Journal of High Energy Physics **2023** (2023), ISSN: 1029-8479, URL: http://dx.doi.org/10.1007/JHEP07(2023)073 (cit. on p. 1).

[8] J. Alwall et al., *The automated computation of tree-level and next-to-leading order differential cross sections, and their matching to parton shower simulations*, Journal of High Energy Physics **2014** (2014), ISSN: 1029-8479, URL: http://dx.doi.org/10.1007/JHEP07(2014)079 (cit. on pp. 1, 9, 19).

[9] R. Frederix et al., *The automation of next-to-leading order electroweak calculations*, Journal of High Energy Physics **2018** (2018), ISSN: 1029-8479, URL: http://dx.doi.org/10.1007/JHEP07(2018)185 (cit. on pp. 1, 9, 19).

[10] P. Artoisenet et al., *A framework for Higgs characterisation*, Journal of High Energy Physics **2013** (2013), ISSN: 1029-8479, URL: http://dx.doi.org/10.1007/JHEP11(2013)043 (cit. on pp. 1, 10, 19).

[11] P. de Aquino and K. Mawatari, *Characterising a Higgs-like resonance at the LHC*, 2013, arXiv: 1307.5607 [hep-ph], URL: https://arxiv.org/abs/1307.5607 (cit. on pp. 1, 10, 19).

[12] Super-Kamiokande Collaboration, *Evidence for Oscillation of Atmospheric Neutrinos*, Phys. Rev. Lett. **81** (8 1998) 1562, URL: https://link.aps.org/doi/10.1103/PhysRevLett.81.1562 (cit. on p. 2).

[13] S. Navas et al., *Review of particle physics*, Phys. Rev. D **110** (2024) 030001 (cit. on pp. 2, 3).

[14] B. Povh, K. Rith, C. Scholz, F. Zetsche and W. Rodejohann, *Teilchen und Kerne Eine Einführung in die physikalischen Konzepte*, Springer Spektrum, 2014, ISBN: 9783642378218 (cit. on pp. 2–4, 6).

[15] J. H. Christenson, J. W. Cronin, V. L. Fitch and R. Turlay, *Evidence for the 2π Decay of the K_2^0 Meson*, Phys. Rev. Lett. **13** (4 1964) 138, URL: https://link.aps.org/doi/10.1103/PhysRevLett.13.138 (cit. on p. 3).

[16] W. Commons, *File:Standard Model of Elementary Particles.svg — Wikimedia Commons, the free media repository*, [Online; accessed 5-February-2026], 2026, URL: https://commons.wikimedia.org/w/index.php?title=File:Standard_Model_of_Elementary_Particles.svg&oldid=1156962948 (cit. on p. 3).

[17] F. Englert and R. Brout, *Broken Symmetry and the Mass of Gauge Vector Mesons*, Phys. Rev. Lett. **13** (9 1964) 321, URL: https://link.aps.org/doi/10.1103/PhysRevLett.13.321 (cit. on p. 3).

[18] P. W. Higgs, *Broken Symmetries and the Masses of Gauge Bosons*, Phys. Rev. Lett. **13** (16 1964) 508, URL: https://link.aps.org/doi/10.1103/PhysRevLett.13.508 (cit. on p. 3).

[19] A. Denner, S. Heinemeyer, I. Puljak, D. Rebuzzi and M. Spira, *Standard model Higgs-boson branching ratios with uncertainties*, The European Physical Journal C **71** (2011), ISSN: 1434-6052, URL: http://dx.doi.org/10.1140/epjc/s10052-011-1753-8 (cit. on p. 4).

[20] ATLAS Collaboration, *Differential cross-section measurements of Higgs boson production in the $H \to \tau^+\tau^-$ decay channel in pp collisions at $\sqrt{s} = 13$ TeV with the ATLAS detector*, JHEP **03** (2025) 010, arXiv: 2407.16320 [hep-ex] (cit. on pp. 4, 5, 11).

[21] M. Hübner, *Higgs Boson Production Cross-Section Measurements in the Di-Tau Final State at ATLAS*, URL: https://bonndoc.ulb.uni-bonn.de/xmlui/bitstream/handle/20.500.11811/9734/6567.pdf?sequence=1&isAllowed=y (visited on 16/02/2026) (cit. on p. 4).

[22] T. Biekötter, A. Grohsjean, S. Heinemeyer, C. Schwanenberger and G. Weiglein, *Possible indications for new Higgs bosons in the reach of the LHC: N2HDM and NMSSM interpretations*, The European Physical Journal C **82** (2022), ISSN: 1434-6052, URL: http://dx.doi.org/10.1140/epjc/s10052-022-10099-1 (cit. on p. 5).

[23] M. V. Sadovskii, *Quantum Field Theory*, Walter De Gruyter GmbH, Berlin/Boston, 2013, ISBN: 978-3-11-027035-8 (cit. on pp. 5, 6, 20).

[24] O. Philipson, *Quantenfeldtheorie und das Standardmodell der Teilchenphysik Eine Einführung*, Springer Spektrum Berlin, Heidelberg, 2025, ISBN: 978-3-662-70849-1 (cit. on p. 6).

[25] *LHC The guide*, URL: https://cds.cern.ch/record/2809109/files/CERN-Brochure-2021-004-Eng.pdf (visited on 14/01/2026) (cit. on p. 7).

[26] *The Large Hadron Collider*, URL: https://home.cern/science/accelerators/large-hadron-collider (visited on 14/01/2026) (cit. on p. 7).

[27] *The ATLAS Detector*, URL: https://atlas.cern/Discover/Detector (visited on 14/01/2026) (cit. on pp. 7, 8).

[28] *Magnet System*, URL: https://atlas.cern/Discover/Detector/Magnet-System (visited on 14/01/2026) (cit. on pp. 7, 8).

[29] *The Inner Detector*, URL: https://atlas.cern/Discover/Detector/Inner-Detector (visited on 14/01/2026) (cit. on p. 7).

[30] *Calorimeter*, URL: https://atlas.cern/Discover/Detector/Calorimeter (visited on 14/01/2026) (cit. on p. 8).

[31] *Muon Spectrometer*, URL: https://atlas.cern/Discover/Detector/Muon-Spectrometer (visited on 14/01/2026) (cit. on p. 8).

[32] T. Wlodek, *Monte Carlo methods in HEP, University of the Great State of Texas*, URL: http://www-hep.uta.edu/~yu/teaching/summer02-5391/lectures/tomasz-061702.pdf (visited on 09/02/2026) (cit. on p. 9).

[33] S. Gieseke, *Introduction to Monte Carlo Event Generators, Lectures at MCnet Vietnam summer school ICISE, Quy Nhon, Vietnam 16/9–20/9 2019*, URL: https://indico.cern.ch/event/796134/contributions/3560243/attachments/1908781/3153323/lect1and2.pdf (visited on 09/02/2026) (cit. on p. 9).

[34] L. Darmé et al., *UFO 2.0: the 'Universal Feynman Output' format*, The European Physical Journal C **83** (2023), ISSN: 1434-6052, URL: http://dx.doi.org/10.1140/epjc/s10052-023-11780-9 (cit. on p. 9).

[35] A. Alloul, N. D. Christensen, C. Degrande, C. Duhr and B. Fuks, *FeynRules 2.0— A complete toolbox for tree-level phenomenology*, Computer Physics Communications **185** (2014) 2250, ISSN: 0010-4655, URL: http://dx.doi.org/10.1016/j.cpc.2014.04.012 (cit. on p. 10).

[36] P. de Aquino, W. Link, F. Maltoni, O. Mattelaer and T. Stelzer, *ALOHA: Automatic libraries of helicity amplitudes for Feynman diagram computations*, Computer Physics Communications **183** (2012) 2254, ISSN: 0010-4655, URL: http://dx.doi.org/10.1016/j.cpc.2012.05.004 (cit. on p. 10).

[37] C. Bierlich et al., *A comprehensive guide to the physics and usage of PYTHIA 8.3*, 2022, arXiv: 2203.11601 [hep-ph], URL: https://arxiv.org/abs/2203.11601 (cit. on p. 10).

[38] A. Buckley et al., *LHAPDF6: parton density access in the LHC precision era*, The European Physical Journal C **75** (2015), ISSN: 1434-6052, URL: http://dx.doi.org/10.1140/epjc/s10052-015-3318-8 (cit. on p. 10).

[39] *Introduction to MC Production*, URL: https://atlassoftwaredocs.web.cern.ch/analysis-software/AnalysisSWTutorial/mc_intro/ (visited on 09/02/2026) (cit. on p. 10).

[40] *The Higgs Characterisation model*, URL: https://cp3.irmp.ucl.ac.be/projects/feynrules/wiki/HiggsCharacterisation (visited on 16/01/2026) (cit. on p. 10).

List of Figures

List of Tables